Characteristics of the Ambient Seismic Field on a Large-*N* Seismic Array in the Vienna Basin

Sven Schippkus*[1], Mikaël Garden[2], and Götz Bokelmann[1]

Abstract

The ambient seismic field is now routinely used for imaging and monitoring purposes. Most commonly, applications aim at resolving crustal-scale features and utilize ocean-generated surface waves. At smaller scales and at frequencies above the microseismic peaks, local sources of seismic energy, often anthropogenic, are dominant, and understanding of their contributions to the ambient seismic field becomes important to apply ambient noise techniques. This study uses data of an industrial-scale seismic deployment covering $\sim$500 km^2 with 10,532 stations, each equipped with several collocated 10 Hz geophones, to provide unique insight into anthropogenic sources of seismic energy in a suburban-to-rural area. We compute amplitude levels, their distance dependency, power spectral densities, and spectrograms to describe the source characteristics. The sources we observe in great detail include windmills, a railway track and trains, cars, oil pumpjacks, power lines, gas pipelines, and airplanes. These sources exhibit time-dependent behavior that is illustrated strikingly by videos of amplitude levels in certain frequency bands that we provide as supplemental material. The data described in this study are a potential resource for future studies, such as automatic signal classification, as well as underground imaging using microseismic noise or the sources presented here.

Cite this article as Schippkus, S., M. Garden, and G. Bokelmann (2020). Characteristics of the Ambient Seismic Field on a Large-*N* Seismic Array in the Vienna Basin, *Seismol. Res. Lett.* **XX**, 1–14, doi: 10.1785/0220200153.

Supplemental Material

Introduction

Dense arrays of hundreds to thousands of seismic stations are common in industrial applications, mostly for exploration of fossil resources. Recently, these arrays have become subject of scientific research, as they allow unique insights that are usually unattainable through scientific funding opportunities. The maturing of ambient noise techniques allows these techniques to become a routine part of seismologists' toolkit (Nakata *et al.*, 2019, and references therein); applying them at local scale is a next natural step (e.g., Mordret *et al.*, 2013, 2018; de Ridder and Biondi, 2015; Nakata *et al.*, 2015; Meng and Ben-Zion, 2018; Spica *et al.*, 2018; Brenguier *et al.*, 2020; Mordret *et al.*, 2020). In recent years, it has become increasingly clear that the description and analysis of seismic sources that generate the ambient seismic field are essential aspects to advance the field in the future (e.g., Karplus and Schmandt, 2018, and references therein).

At frequencies below 1 Hz, ocean-driven mechanisms have been identified and described that continuously induce seismic noise that is measured all around the globe (Longuet-Higgings, 1950; Hasselmann, 1963; Ardhuin *et al.*, 2011). Ardhuin *et al.* (2011) classify these mechanisms into primary (wave-to-land interaction) and secondary (wave-to-wave interaction), providing explanations for the primary ($T \sim 14$ s) and secondary ($T \sim 7$ s) microseismic peaks, as well as the Earth's hum at periods $T > 30$ s. In central Europe, the dominant sources are located in the North Atlantic (Juretzek and Hadziioannou, 2016, 2017). These lower microseismic frequencies are now routinely used for imaging (e.g., Lin *et al.*, 2008; Roux, 2009; Ren *et al.*, 2013; Kästle *et al.*, 2018; Lu *et al.*, 2018; Schippkus *et al.*, 2018) and monitoring (e.g., Brenguier *et al.*, 2008, 2014; Lecocq *et al.*, 2017) of the subsurface.

At frequencies above 1 Hz, dominant seismic sources in populated areas are generally of anthropogenic nature. Traffic and machinery, in particular, have been shown to induce strong signals that may dominate the seismic recordings at certain frequencies, and efforts have been made to discriminate and understand the contributors to the ambient seismic field at these frequencies (e.g., Nakata *et al.*, 2015; Riahi and Gerstoft, 2015; Stammler and Ceranna, 2016; Fuchs *et al.*, 2017; Inbal *et al.*, 2018; Meng and Ben-Zion,

1. Department of Meteorology and Geophysics, University of Vienna, Vienna, Austria; 2. Department of Geophysics, OMV E&P GmbH, Vienna, Austria

*Corresponding author: sven.schippkus@univie.ac.at

2018; Brenguier *et al.*, 2019). These sources are usually thought to degrade station performance of permanent networks, for example, when new windmills are installed near a long-operating seismic array (Stammler and Ceranna, 2016). Riahi and Gerstoft (2015) used data of the Long Beach seismic array (5200 geophones) to describe traffic-generated seismic noise, including Metro trains, cars, and airplanes, in an urban region. Brenguier *et al.* (2019) were able to utilize such anthropogenic sources, in their case trains, for seismic monitoring of the San Jacinto fault zone. It is clear that a good understanding of the ambient seismic field is essential for this kind of application. In addition to anthropogenic sources, wind interaction with vegetation or other obstacles can be a significant source at higher frequencies (Dybing *et al.*, 2019; Johnson *et al.*, 2019). Dybing *et al.* (2019) argue that seismograms can instead be dominated by anthropogenic sources at these higher frequencies, in particular, near-populated areas, such as our study region.

This study aims at giving insight into the complexities of the ambient seismic field in a suburban-to-rural area with windmills, train traffic, oil pumpjacks, and other sources of seismic energy. For this, we use data of a dense seismic array (10,532 stations) that was deployed for 1 week in the eastern Vienna basin, near Gänserndorf, to discriminate, characterize, and describe the properties of these anthropogenic sources. This study is further intended as a reference for future studies, such as ambient noise tomography at shallow depths. The data may also become a potential benchmark dataset for new and established signal-classification algorithms, a field that is advancing rapidly in recent years due to the advent of machine learning techniques (e.g., Kong *et al.*, 2018; Chamarczuk *et al.*, 2019).

Experiment Setup and Data

The study area is located just west of the Austria–Slovakia border in the Vienna basin around the city of Gänserndorf (Fig. 1). The stations partially cover the Matzen oil field in the northwest, which has been in production since 1949 with 12,300 barrels of oil per day and a total proven reserve of 510 million barrels (Brix and Schultz, 1993). The main purpose of the seismic survey was active seismic exploration (Garden and Zuhlsdorff, 2019).

The 10,532 seismic stations were set up with 40 m in-line and 400 m cross-line spacing, with a north-northeast to south-southwest in-line orientation, and minor deviations from the planned lines (Fig. 1). Each seismic station is equipped with 12 or 24 densely collocated (within 1 m^2) vertical-component 10 Hz geophones (Sercel JF-20DX). In total, ~150,000 geophones were deployed for this survey. The data at each station are stacked before being recorded by autonomous nodal digitisers (AutoSeis High Definition Recorder [HDR]) at 500 Hz sampling rate. Prior to the start of active measurements, the stations recorded the ambient seismic field, that is, the data used in this study. The data were recorded over the course of 6 days from 18 to 23 January 2018 during daytime only,

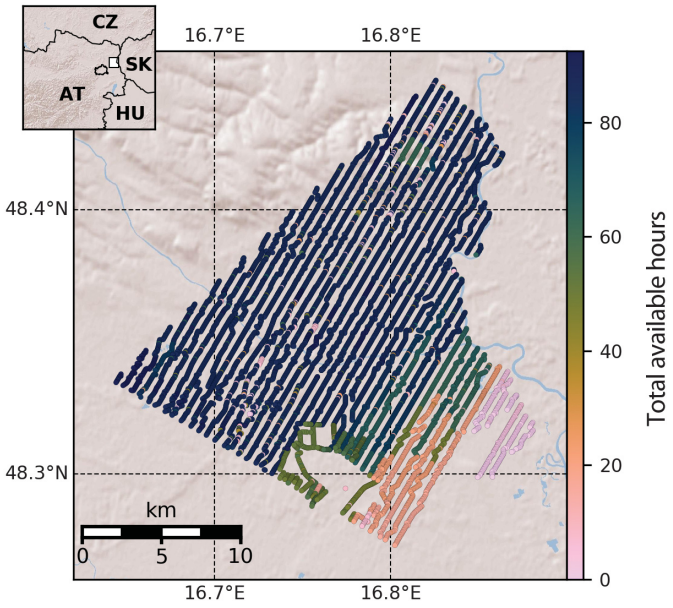

Figure 1. Map of the study area at the Austria–Slovakia border, just northeast of Vienna (see inset). The array consists of 10,532 stations with 40 m in-line- and 400 m cross-line spacing. Data are available for up to 92.5 hr and were recorded from 18 to 23 January 2018 (during daytime only).

from 06:30 to 22:00 local time (UTC+1). That way, the stations recorded up to 92.5 hr of data. The stations in the southeast of the study area were deployed during the measurement and have data available for as little as 12 min (Fig. 1).

The array has a number of faulty stations that did not record usable data. Those stations were dominated by artifacts and glitches; we do not use the data from those stations further. We identify those stations by extremely high power spectral densities (PSDs; higher than 1E12 $c^2\,m^2/s^2$ Hz) at frequencies between 0.1 and 1 Hz. A total of 816 (7.7%) stations are classified as faulty. Thanks to the size of the array with 10,532 total stations, excluding 816 stations that are randomly distributed throughout the array has negligible impact on our analysis. The fact that 12 or 24 geophones are collocated and stacked increases signal-to-noise ratio significantly, because self-noise is mitigated. This, however, may also make stations potentially unsuable if only one of those geophones is faulty.

We removed the instrument response of the geophones from the data, but a scaling factor for the (unknown) transfer function of the AutoSeis HDR digitisers remains. Thus, amplitudes are given in c times meters per second, in which c represents the conversion from counts (output of the digitiser) to Volts (output of the geophone), and not directly in physical units of ground motion.

The study area includes a remarkable breadth of potential sources of seismic signals that allow unique insight into their properties. The area encompasses cities and towns, the main

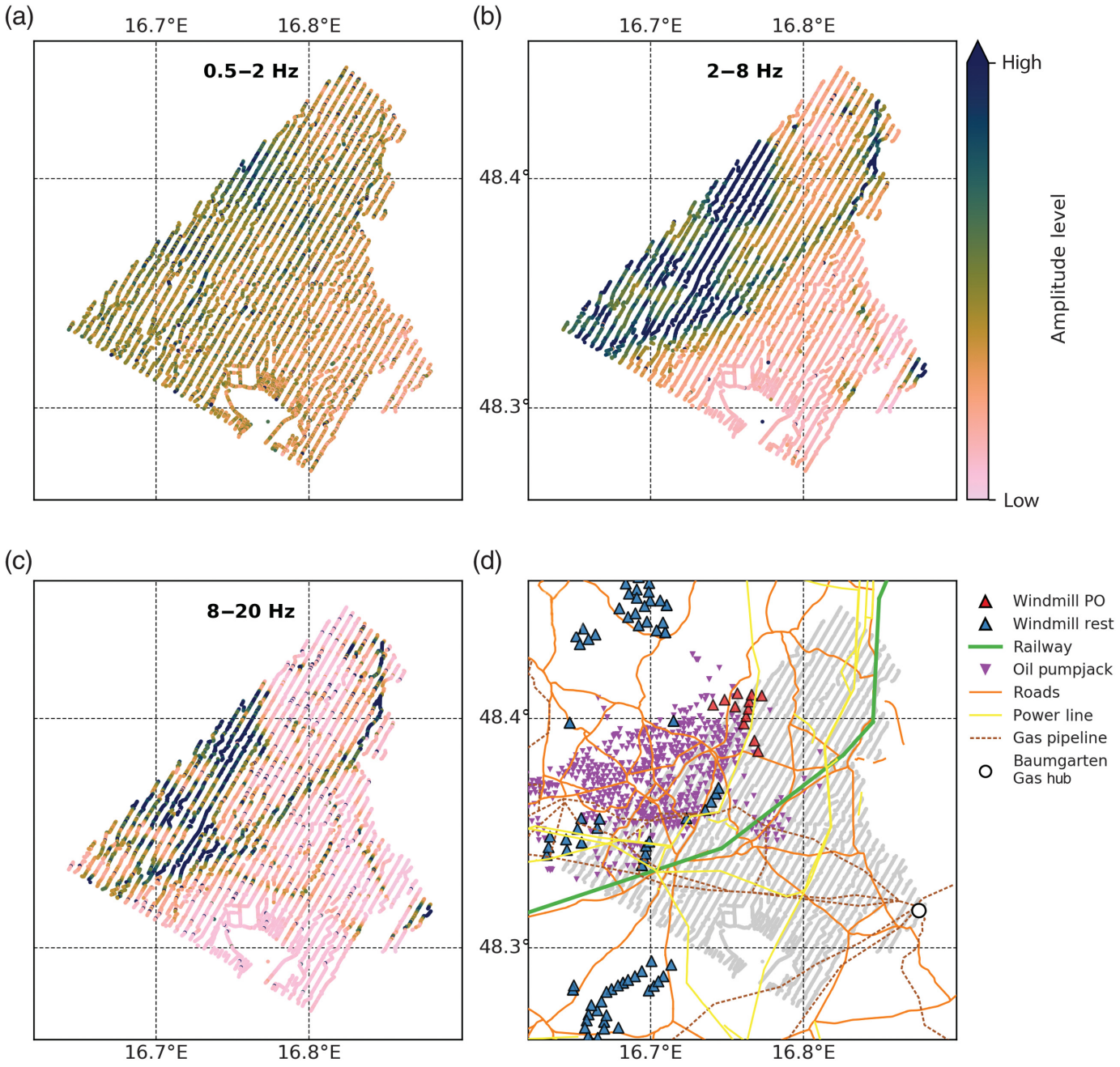

railway track that connects Vienna to the Czech Republic, dozens of windmills, hundreds of oil pumpjacks, power lines, the Baumgarten gas hub (Schneider *et al.*, 2018) and underground gas pipelines, car and truck traffic on roads (see Fig. 2), as well as airplane traffic of the nearby Vienna International Airport. We do not treat cities and towns as individual potential noise sources, because they are ultimately an amalgamation of various sources such as traffic, people, and machinery. Separating their individual contributions at this close distance is not straightforward and exceeds the scope of this article.

Figure 2. Mean noise amplitudes in three frequency bands (a–c) and potential noise sources in the study area (d). (a) At 0.5–2 Hz, relatively even distribution of amplitudes with slightly increased amplitude levels in the north, close to the wind farm Prottes–Ollersdorf (PO). (b) At 2–8 Hz, increased amplitudes along a number of low-frequency noise sources: railway track, wind farm PO, oil pumps, and the Baumgarten gas hub. (c) At 8–20 Hz, roads and power lines emerge as visible noise sources, and increased amplitudes are spatially focused. (d) Map of potential noise sources in the study region. Locations of sources extracted and compiled from OpenStreetMap contributors (2017), Interessengemeinschaft Windkraft Österreich (2020), Gas Connect Austria GmbH (2020), and OMV E&P GmbH (personal comm., 2020).

Results

To gain insight into the properties of each of the noise sources recorded on the array, we perform five analyses: mean absolute

amplitudes recorded at each station as a function of time provide insight into the spatial and temporal distribution of sources, including moving sources such as trains. PSDs of stations that are located close to noise sources reveal the spectral characteristics of the sources, especially stationary ones like windmills and oil pumpjacks. PSD amplitudes versus distance allow to study the distance-dependent impact of those noise sources at certain frequencies and propagation regimes. Spectrograms of particularly well-recorded events and continuous sources provide further detailed insight into their characteristics. Beamforming at frequencies near the secondary microseismic peak illustrates the capability of the 10 Hz geophones to reliably record such frequencies and their potential for classical ambient noise applications.

We computed mean absolute amplitudes for all stations in 1 min time windows for the available time frame for unfiltered and filtered (in three frequency bands: 0.5–2, 2–8, 8–20 Hz) data. Maps of the amplitude levels averaged over the entire duration of deployment (Fig. 2a–c) reveal a spatially consistent distribution of amplitude levels that can be attributed to noise sources in the study area (Fig. 2d). Locations of sources are extracted and compiled from OpenStreetMap contributors (2017), Interessengemeinschaft Windkraft Österreich (2020), Gas Connect Austria GmbH (2020), and OMV E&P GmbH (personal comm., 2020).

At 0.5–2 Hz, we observe a generally even distribution of amplitudes. Stations record slightly increased amplitude levels in the northwest, near the wind farm Prottes–Ollersdorf (PO; red triangles in Fig. 2d). At 2–8 Hz, we additionally observe increased amplitudes near the railway track, oil pumpjacks, and the Baumgarten gas hub. At 8–20 Hz, roads and power lines emerge as visible noise sources, in addition to the sources visible at lower frequencies.

Videos of the mean absolute amplitudes with 1 min time resolution provide a unique and remarkably clear illustration of daily activity in the study area (Text S1 and Videos S1–S4, available in the supplemental material to this article). We observe increased noise levels and more moving sources, such as cars and trains, during weekdays, and less activity on the weekend. The wind farm PO emerges as a dominant noise source with time-variable activity. In contrast, the other windmills in the study area (blue triangles in Fig. 2d) appear to generate significantly less seismic signal (Videos S1–S4). Oil pumpjacks in the region (purple inverted triangles in Fig. 2d) induce increased amplitude levels at frequencies above 2 Hz and are one of the dominant sources at these frequencies (Videos S3 and S4). The spatial distribution of high-amplitude levels in the northwest matches particularly well with the locations of the wind farm PO and oil pumpjacks (Fig. 2 and Videos S3 and S4). In addition to anthropogenic sources, the videos also visualize weather-related events (Text S1, Fig. S3, Video S2).

Binned and stacked PSDs for stations' near potential noise sources (i.e., within 200 m distance) exhibit distinct spectral features that can be attributed to the respective noise sources (Fig. 3). Stations near windmills (Fig. 3a,b) show clear spectral peaks and increased amplitudes at frequencies from 1 to 10 Hz, and stations near the railway track (Fig. 3c) and roads (Fig. 3e) have smoother spectra ("less peaky") and increased amplitudes at frequencies above 10 Hz. Stations near power lines (Fig. 3f) and gas pipelines (Fig. 3g) show two distinct trends between 2 and 10 Hz. Stations that are not near any of the identified noise sources (i.e., in at least 1000 m distance) show clearly lower amplitudes across all frequencies above 1 Hz. At frequencies below 1 Hz, amplitudes increase with decreasing frequency. This is representative of the increasing impact of self-noise and not necessarily to be understood as seismic signal.

To ensure that there is no significant cross-contamination between the different sources and their impact on the PSDs for the following interpretation, we additionally limit the set of stations attributed to a single source to stations that are not within 400 m of any other noise sources (Fig. S2). This selection further focuses the PSD distributions, especially those of stations near oil pumpjacks, power lines, and gas pipelines, as they are often located in close proximity to other sources (e.g., oil pumpjacks near roads) or are relatively weak. This selection also implicitly excludes cities and town centers, as there are multiple sources nearby in more densely populated areas. However, this selection does eliminate a considerable amount of stations for further analyses, and, in the case of stations near windmills that are not part of the wind farm PO, all of them (Fig. S2b). Still, these stations show particularly distinguishable spectral features not seen on other stations, even when including other nearby sources (Fig. 3). The exclusion of stations near other sources can be detrimental for stations near strong persistent sources, such as windmills, but appears to be useful for stations near weak and broadly distributed sources, such as power lines. Therefore, both approaches (exclusion vs. no exclusion) provide important insight and are useful for discussion.

Regardless of this selection, stations appear to reliably recover signals as low as 0.2 Hz. There are a number of low-amplitude peaks from 0.2 to 1 Hz observed across essentially all stations with similar amplitudes. Above 1 Hz, spectral signatures of each source start to dominate the spectra of stations near those sources.

PSD amplitudes as a function of distance at certain frequencies reveal distinctly different patterns for different noise sources (Fig. 4). Here, we exclude stations within 400 m to any other source to reduce some of the cross-contamination between different sources, and still allowing us to fit the data reliably. Wherever we do observe a distance-dependent decay of amplitudes, they appear to follow a power-law description (black lines in Fig. 4), which we fit using nonlinear least squares without additional outlier removal. The power-law exponent describes the propagation geometry of the recorded signal (spherical vs. cylindrical), and thus may give insight into

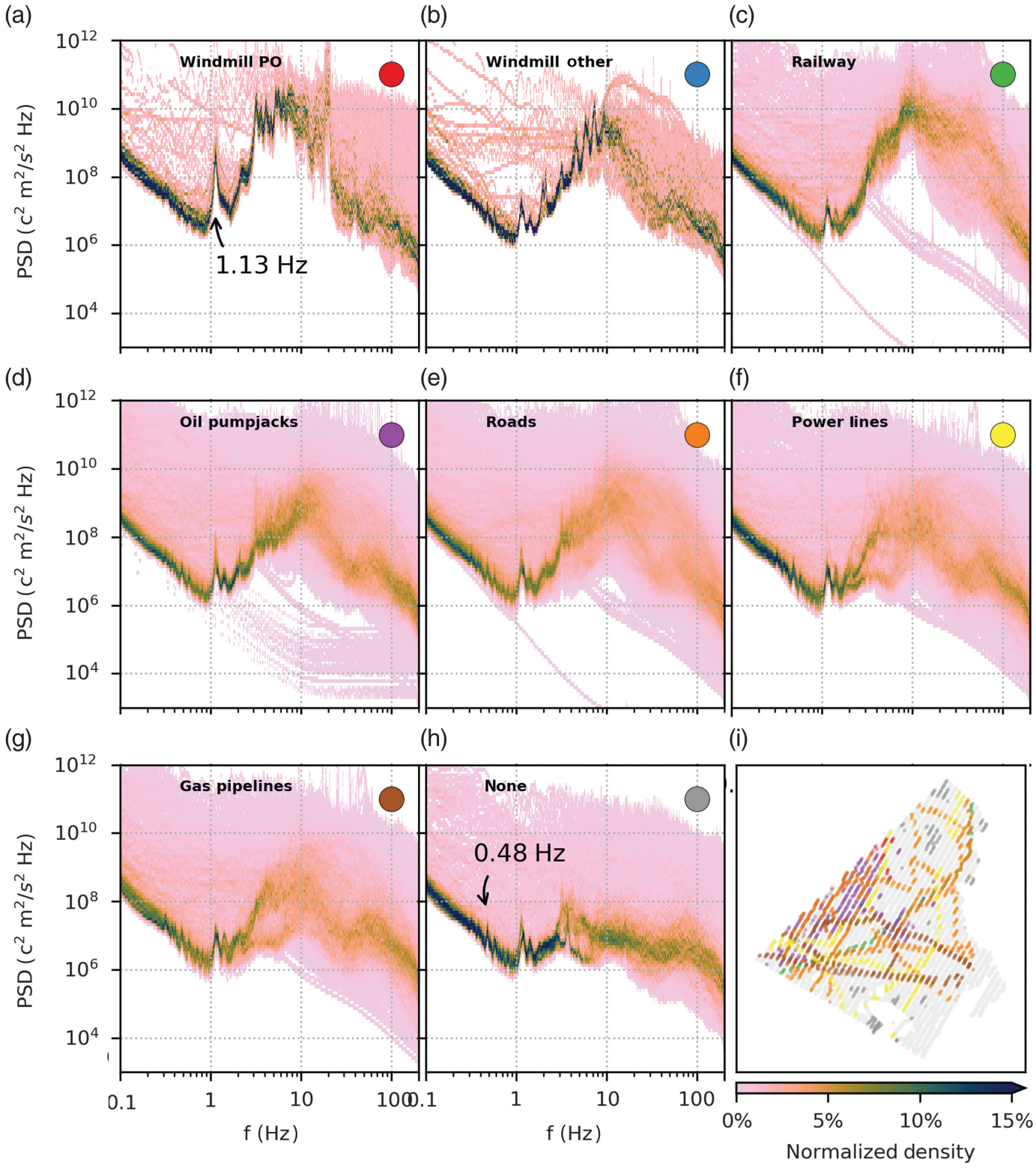

Figure 3. Binned and stacked power spectral densities (PSDs) for stations close to the noise sources mapped in Figure 2d, normalized by the total number of stations. The sources are: windmills of (a) wind farm PO, (b) other windmills, (c) the railway track, (d) oil pumps, (e) roads, (f) power lines, and (g) gas pipelines. Nearby stations are defined as within 200 m distance to a given noise source. Stations labeled "none" (h) are in at least 1000 m distance to any noise source. The map view (i) shows the spatial distribution of stations selected for the respective noise sources by color.

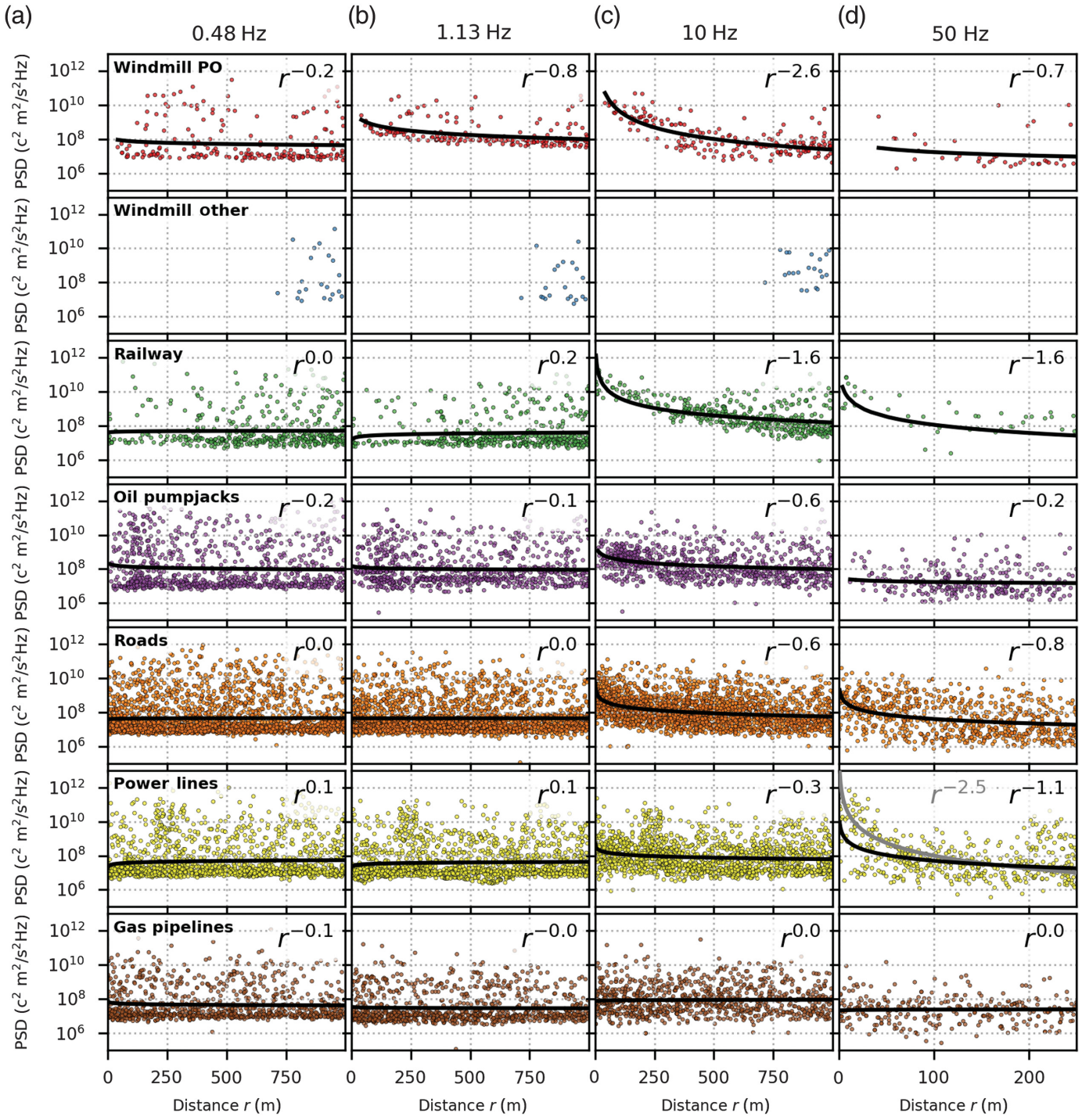

Figure 4. PSD amplitudes versus distance for the known noise sources at (a) 0.48 Hz, (b) 1.13 Hz, (c) 10 Hz, and (d) 50 Hz. At 0.48 Hz, no source exhibits a clear decay with distance. At 1.13 Hz, the windmills of PO appear as the only significant noise source that exhibit a distance-dependent decay of amplitude. At 10 Hz, pronounced amplitude decay for windmills of PO, the railway track, oil pumps, and roads. At 50 Hz, sharp decline in amplitude over short distances for stations near the the railway track, roads, and power lines. Note that at 50 Hz data are shown up to 250 m distance, instead of 1000 m. Data were fit with power laws (solid lines). The gray lines mark the amplitude decay when excluding stations that do not show increased amplitudes near power lines at 50 Hz.

its source mechanism. At 0.48 Hz, no source appears to induce a significant distance-dependent decay. Windmills of PO have significant impact on stations in up to a few hundred meters distance at 1.13 Hz (Fig. 4). At 10 Hz, we observe significant impact of windmills of PO and the railway track on stations up to 1 km distance. Other sources, such as oil pumpjacks and roads, induce increased amplitude in up to a few hundred meters distance. Power lines appear to generate seismically recorded signal up to tens of meters away. At 50 Hz, the frequency of the power grid, power lines become one of the most significant sources for stations up to 100 m away. The signal recorded near other sources (windmills of PO, railway, oil pumpjacks, and roads) also decays rapidly down to background-noise levels over tens to a few hundreds of meters (Fig. 4). It is clear that the distance up to which sources are relevant depends on the seismic energy emitted by the source, the propagation regime, and the level of background noise.

Representative spectrograms of 10 min windows provide further insight into the spectral and temporal properties of the different noise sources (Fig. 5). We show spectrograms for the wind farm PO (Fig. 5a), a different windmill (Fig. 5b), trains (Figs. 5c and 6a), an oil pumpjack (Figs. 5d and 6b), cars (Fig. 5e), a power line (Fig. 5f), a gas pipeline (Fig. 5g), no nearby source (Fig. 5h), and an airplane (Fig. 5i). Some sources excite energy continuously over time scales of tens of minutes to hours and even days, such as wind mills, oil pumpjacks, power lines, and potentially gas pipelines. Other sources are distinct events, such as passing trains, cars, and airplanes.

We perform beamforming at frequencies near the secondary microseismic peak at 0.2–0.5 Hz (Text S1 and Fig. S1). At these frequencies, there appears to be no major source inside the array or very close by, and the plane-wave assumption of classical beamforming is likely reasonable. We find that the array records seismic energy arriving from northwest (301°, 3.4 km/s), consistent with ocean-generated Rayleigh waves in the North Atlantic (Juretzek and Hadziioannou, 2016, 2017). At higher frequencies, this assumption does not hold any longer, and we do not compute beam powers for them. At lower frequencies, we do not retrieve coherent signals, and the beamforming results become unreliable.

Discussion

We are able to clearly distinguish the seismic characteristics of several anthropogenic sources in the study area (Figs. 2–6). However, our analysis and following discussion are based on the assumptions that (1) we have identified and mapped all relevant sources of seismic signal in the area, (2) sources of a given type have similar characteristics, (3) site effects are not important, and (4) that, we have sufficiently eliminated cross-contamination of nearby sources, where necessary. In the following, we first discuss each of those assumptions before discussing each source in greater detail.

The locations of seismic sources are extracted and compiled from several sources, and some may be prone to errors. Locations of windmills (Interessengemeinschaft Windkraft Österreich, 2020) are precise, and additional information about the windmill model is available. Infrastructure data, such as roads, railway tracks, and power lines, are extracted directly from data provided by OpenStreetMap Contributors (2017). Although this data is crowdsourced and relies on the general public for accuracy, it is generally considered to be precise and rich in detail. The locations of gas pipelines we use in this study are based on the online map provided by Gas Connect Austria GmbH (2020). We may have introduced location errors up to tens of meters during the extraction of this information, as this was done visually. Oil pumpjack locations are precise, but include all locations in the area. There is no distinction between active and inactive pumpjacks. We believe these sources to be the entirety of relevant seismic sources in the region, and our analysis has not given any indication that we may have neglected other major sources.

We assume that all individual sources of a given type behave similarly, which for some sources is clearly invalid. The distribution of PSDs for power lines and gas pipelines shows two-to-three distinctly emerging maxima between 2 and 10 Hz (Fig. 3f,g). Similarly, amplitudes at 50 Hz for stations near power lines (Fig. 4) show that some stations do not follow a power-law decay of amplitudes with distance and instead are at background levels of noise even close to the power lines. Distinct source events, such as trains and cars, are obviously also dependent on the individual source itself (e.g., freight train vs. passenger train, or different cars, see Fig. 5 and supplemental material). These considerations are indeed what lead to the distinction between the windmills of the wind farm PO and other windmills, as these expose different characteristics across every measure we analyze in this study (Figs. 2–5). Therefore, caution is advised when interpreting our findings, in particular, patterns that may be explained simply by different realizations of the same source type.

We further neglect the potential impact of site effects on recorded amplitudes. At large scale, the entire study region is covered with Quaternary sediments, and there are no hard rock sites. At smaller scale, very local effects such as poor coupling of sensors and soil properties may impact station performance and thus recorded amplitudes. We do, in fact, find that a few percent of stations (depending on frequency) show very high amplitudes compared to others (Figs. 3 and 4), and these do not appear to correlate with any known noise source. However, they also do not form a spatially coherent picture and appear to be distributed randomly throughout the array. Therefore, these stations are likely not indicative of geophysical site effects and are more likely to have poor coupling or data-quality issues. These stations should, therefore, not be considered in the following interpretation and discussion, and a stricter or more elaborate selection of stations may enhance some insights.

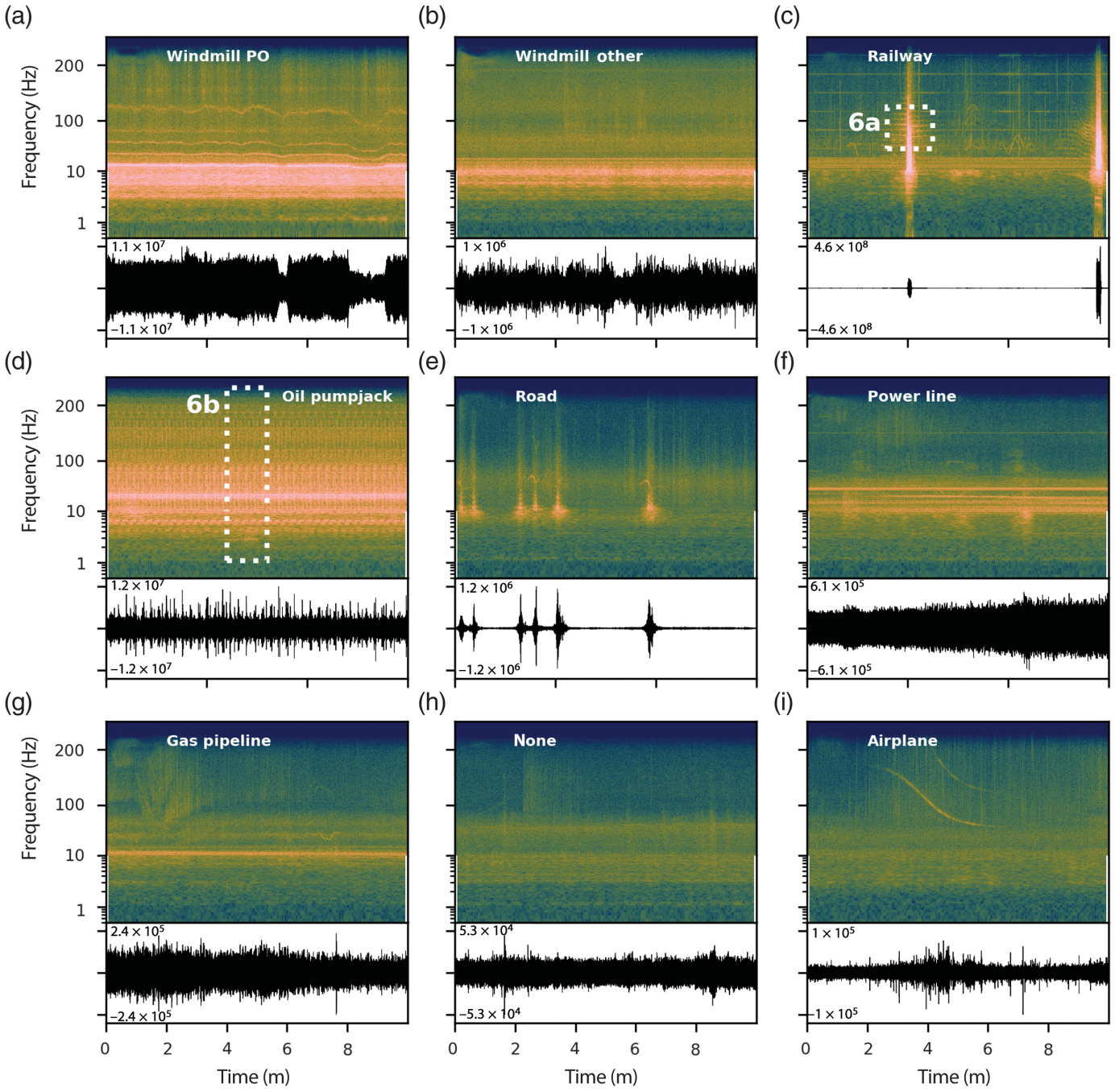

To eliminate cross-contamination between different sources, we put constraints on the stations included for analysis of a given source by distance to any other source. We chose a 400 m distance threshold as a compromise to balance that sources are often located close by to other sources and that only few sources show significant impact at greater distances, namely windmills of PO and the railway track at 10 Hz (Fig. 4). A stricter threshold would exclude a very large number of stations from our analyses and thus reduces our ability to observe consistent trends, while not providing new insights.

Figure 5. Representative spectrograms (2 s windows above 10 Hz, 10 s windows below 10 Hz, 95% overlap, constant color scale) from 10 min seismograms, for different sources: (a) a windmill of PO, (b) a different windmill, (c) trains, (d) a continuously operating oil pump, (e) cars, (f) a power line, (g) a gas pipeline, (h) no nearby source, and (i) a passing airplane. Some sources continuously excite ground motion (a,b,d,f,g), whereas others are distinct events (c,e,i). The dashed white boxes mark the zoomed-in views in Figure 6.

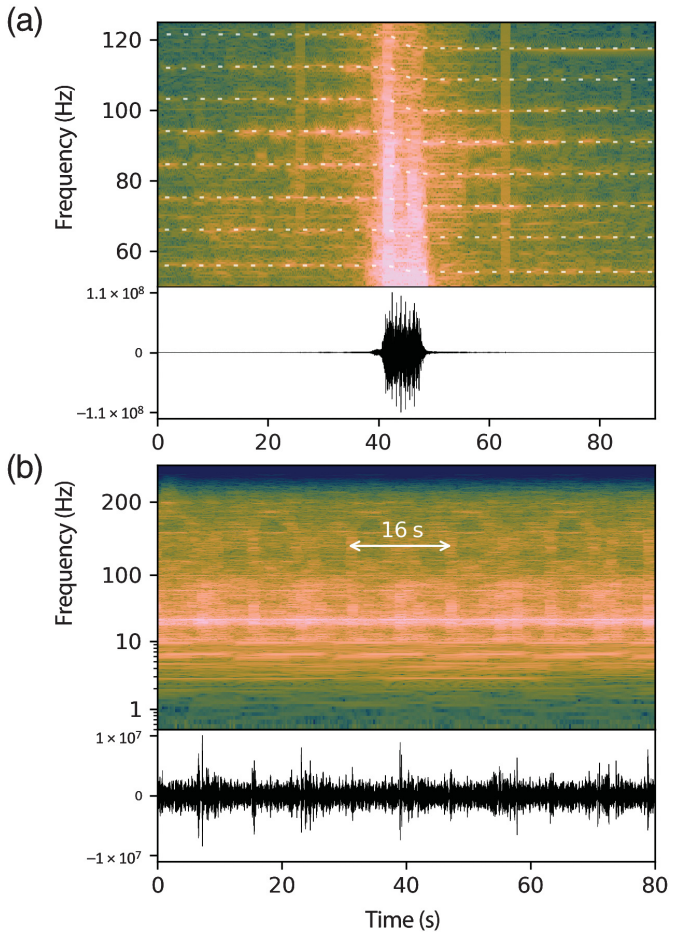

Figure 6. Zoomed-in spectrograms from Figure 5 for (a) a passing train and (b) an oil pump. The spectrogram of the passing train exhibits equidistant spectral lines induced by the passing train, as well as a Doppler shift (white dashed lines, modeled with medium velocity $v_m = 1$ km/s, and train velocity $v_t = 60$ km/hr). The complex and periodically repeating spectrogram of the oil pump is clearly related to the pumping motion with a period of ~16 s.

Therefore, we believe our analysis allows to make reliable observations that relate to the individual anthropogenic seismic sources. In the following, we discuss each of the potential sources, in a sequence of decreasing impact on the ambient seismic field in the study area.

Windmills

As described previously, we differentiate two sets of stations near windmills: those near the wind farm PO (red triangles in Fig. 2d) with 13 windmills and those near other windmills (blue triangles in Fig. 2d). Stations near PO have generally higher amplitudes than all other stations (Figs. 2, 3, and 5) and show different spectral peaks than those near the other windmills (Figs. 3a,b and 5a,b). The prominent spectral peak at 1.13 Hz, recorded on almost all stations of the array, appears to be induced by the windmills of PO, as the peak's amplitude is highest near the windmills (Fig. 3). Similarly, there is a clear amplitude decay with distance for stations near PO at 1.13 and 10 Hz (Fig. 4). However, amplitudes decay down to background-noise levels after about 500 m. We find that at 1.13 Hz, only the windmills of PO show a significant distance-dependent decay of measured amplitudes. The other windmills have only few nearby stations that are not excluded due to the vicinity to other sources (Fig. 4), and we do not observe a conclusive distance-dependent trend at any of the chosen frequencies.

The spectrogram reveals that the windmills of PO often operate at varying frequency (Fig. 5a). Wherever the amplitude is decreased, the dominant spectral peaks shift to lower frequencies. This effect has also been observed by Hu *et al.* (2019). The other windmills induce less seismic energy and appear to operate at constant frequency. The windmills of PO (Enercon E-101) produce 3.05 MW each with a maximum rotation speed of 0.24 revolutions per second (rps) and 50 m long blades, whereas the other windmills (Enercon E-70/E4) produce 1.8 MW each with maximum 0.36 rps and 35 m long blades (Interessengemeinschaft Windkraft Österreich, 2020). Furthermore, Enercon E-101 windmills can start operation at lower wind speeds than E-70/4 (2.0 vs. 2.5 m/s). It is, therefore, not surprising that the windmills of PO induce more seismic energy due to operation at lower wind speeds, longer blades, and higher energy output. Similarly, it is not surprising that they induce different spectral peaks (Fig. 5a,b). The 0.48 Hz peak visible across all stations (Fig. 3) may possibly be attributed to the first overtone of the maximum rotation speed of Enercon E-101 windmills (0.24 Hz), but we do not find a conclusive distance-dependent amplitude decay at this frequency (Fig. 4). It is possible that this spectral peak does not decay strongly, because the wavelength of a Rayleigh wave at 0.48 Hz (~5 km) is only slightly smaller than the aperture of the array. In addition, the spectral peak at 1.13 Hz is not an overtone of 0.24 Hz.

Windmills as sources of seismic signal and their impact on the performance of permanent seismic stations have recently become an issue for network operators. Stammler and Ceranna (2016) showed that the seismic energy induced by windmills correlates well with wind speed and contains distinct spectral peaks that overpower the background noise at frequencies of 1–7 Hz. Our observations corroborate this with clear spectral peaks in this frequency range and beyond (Fig. 3a,b).

Stammler and Ceranna (2016) were further able to identify a power-law decay of amplitudes with distance from about 1 up to 8 km distance, the distance of the Gräfenberg array to the newly installed windmills. Our dataset allows insight into the distance-dependent decay from a few meters up to a few kilometers distance, complementing their insight. Our analysis is based on 10 Hz geophones deployed in a suburban-to-rural region and in a sedimentary basin. Therefore, high-amplitude levels are expected throughout the entire array, which may

hinder our ability to estimate amplitude decay precisely. Gortsas *et al.* (2017) modeled the generation of seismic and infrasound noise by windmills numerically. In their model, displacement amplitudes decay with distance from the windmill r by the power law $r^{-0.9}$, similar to surface-wave decay (r^{-1}). This is in contrast to the decay of PSD values reported by Stammler and Ceranna (2016) that follow $r^{-2.7}$, exceeding body-wave decay (r^{-2}). We find two different power-law decay exponents at 1.13 Hz with $r^{-0.8}$ and at 10 Hz with $r^{-2.6}$, potentially representing both propagation regimes. However, the background-noise level is reached after ∼250 m at 1.13 Hz and after ∼750 m at 10 Hz. This may bias our estimate of the power-law decay of windmill-generated seismic energy at 1.13 Hz to be slower than it is in reality. Hu *et al.* (2019) report PSD amplitude decay exponents from −0.52 to −1.87, depending on frequency, and they similarly suggest that this may be related to body-wave (near-field) and surface-wave (far-field) propagation regimes. Their results are based on four stations only though. Edwards (2015) finds surface-wave propagation on four stations at 2.41–4.83 Hz, corresponding to the turbine blade-pass harmonics of the windmill they investigated. It may appear, and our data also suggests, that different propagation regimes are active at different frequencies. We observe cylindrical decay at 1.13 Hz (likely surface waves) and spherical decay at 10 Hz (potentially seismoacoustic propagation). The fact that Stammler and Ceranna (2016) observe spherical decay at 1–8 km distance, however, raises questions about a seismoacoustic mechanism at such long distances, but their results are based on few stations only. In any case, geometrical effects on amplitude decay exceeds the impact of frequency-dependent attenuation considerably and is the likely explanation for the observed trends.

Trains

Trains are moving sources that can be easily identified in the videos of amplitude levels over time (Text S1 and Videos S1–S4). The railway track is the strongest source above 10 Hz (Fig. 3c), and it induces no significant narrowband spectral peaks, different from stations near windmills (Fig. 3a,b). The spectrogram, however, shows clear evidence for a strong influence of the traction current (operated at 16.7 Hz) on the seismic recordings (Fig. 5c). The continuous horizontal lines present throughout the 10 min spectrogram are the first and even overtones of the traction current (first, second, fourth, sixth, … overtone). Odd overtones after the first are either extremely weak or not excited (Fig. 5c), for which we do not have an explanation.

Fuchs *et al.* (2017) have described the spectral features of passenger and freight trains on the same railway track that crosses our study area. They observed equidistant spectral lines and argued that they are likely induced by the interaction of the trains' axles with the railway track as quasistatic sources. Brenguier *et al.* (2019) modeled this interaction and confirmed the quasistatic loading mechanism. The temporary broadband station used by Fuchs *et al.* (2017) is part of the AlpArray project (Hetényi *et al.*, 2018) and located ∼2 km to the west of our array. It is not surprising that we observe the same spectral features they described. Unlike Fuchs *et al.* (2017), however, we do observe a clear Doppler effect for most passing trains. In Figure 6a, we identify and model the frequency shift, as the train passes the seismic station with ∼60 km/hr. Fuchs *et al.* (2017) were limited to a single station in 1.4 km distance to the track, whereas, in our study, we have several stations in distances of tens of meters to the track. Therefore, we are able to observe a clear Doppler effect that is not mitigated by distance to the moving source.

Brenguier *et al.* (2019) demonstrated the capability of train signals being used as a source for seismic monitoring. They correlated train-generated seismic signals to reconstruct body waves that propagate through the San Jacinto fault zone and are thus sensitive to its structure. This can in principle be applied to monitoring of other subsurface features that change seismic properties over time as well, such as the Matzen oil and gas field in our study area.

Oil pumpjacks

Oil pumpjacks continuously generate strong and characteristic seismic signals. In addition to windmills and the railway track, those pumpjacks represent the third major seismic source at 2–20 Hz (Fig. 2b,c). The spatial distribution of increased amplitudes in the northeast at those frequencies is particularly well explained by the presence of oil pumpjacks (Fig. 2d).

Amplitudes peak around 10–20 Hz in the PSDs, with some minor peaks at 1–10 Hz (Fig. 3d). These are likely related to the machinery and the up-and-down motion of those pumpjacks. There are no distinct peaks that can be clearly attributed to the pumpjacks at frequencies below 1 Hz, which one may expect due to their movement. In fact, we do directly observe the periodical motion of an oil pumpjack in the seismic trace and spectrogram of a nearby station (Figs. 5d and 6b), with a repeating period of ∼16 s. The highest amplitude for this station is found at ∼40 Hz, but this peak in the spectrogram is not represented well in the distribution of PSDs (Fig. 3d and Fig. S2d). This is an indication that our oil pumpjack locations are potentially heavily biased toward inactive locations, and that stations near inactive oil pumpjacks may thus dominate the PSDs. In addition, not all locations that are still equipped with oil pumpjacks may be active at all times.

Stations near oil pumpjacks mostly show low amplitude decay rates ($r^{-0.1}$ to $r^{-0.6}$), and the power laws at 0.48 and 1.13 Hz do not appear to describe the actual observed amplitudes well (Fig. 4). Instead, the power-law fit appears to be heavily biased by a number of stations near the oil pumpjacks (at 50–250 m distance) that show increased amplitude levels apparently unrelated to the pumpjacks. At 10 Hz, however, the amplitude decay is quite clear and is more resembling

surface-wave propagation ($r^{-0.6}$, Fig. 4). A few stations show low amplitudes quite close to pumpjacks.

Cars

Stations near the roads show passing cars and trucks that induce seismic signals at frequencies of ~2 Hz and above (Fig. 3 and Fig. S2). PSD amplitudes at these frequencies are among the highest across all sources, surpassed only by stations near the railway track, and with a considerable spread.

Car traffic is not equally distributed among all kinds of roads. For our analysis, we selected all roads except minor roads that are only used very infrequently and mainly for agricultural machinery. There is no highway in the study area. Still, the PSDs show a spread of several orders of magnitude in amplitude for the selected stations, in particular at 10–100 Hz (Fig. 3 and Fig. S2). Simply speaking, a few roads show very high traffic, mostly near Gänserndorf in the west, whereas others see very little traffic (see Text S1 and supplemental material).

Depending on the type of road, and the traffic density on it, cars could also be utilized as continuous seismic sources. In contrast to train traffic, however, it seems that we do not observe a quasistatic loading mechanism, as there are no equidistant spectral lines visible in the spectrograms (Fig. 5e). In addition, cars do not follow a strict schedule that would constitute a reliably repeating source to use for monitoring purposes over time (Brenguier *et al.*, 2019). Still, on high-traffic roads, such as highways, the roads themselves can potentially be seen as a continuously excited noise source; it seems impossible with the current array spacing to distinguish individual cars and their seismic impact during times of high traffic (Riahi and Gerstoft, 2015).

Power lines

The power grid, operating at 50 Hz in Austria, generates strong spectral lines at 50 Hz and its second overtone (150 Hz) on nearby stations (Fig. 5f). This is similar to the observation of the railway traction current, in which we also observe even overtones of the base frequency (Figs. 5c and 6a). It appears certainly possible that the power grid couples electromagnetically into the seismometers over distances of tens of meters due to very high voltages.

However, this does not explain that stations near power lines also exhibit increased amplitudes at frequencies lower than 50 Hz (Figs. 2c and 5f). These stations are located mostly in fields, such as the ones at around 48.33° N, 16.8° E, in which there is no other seismic source nearby. The amplitude video for 8–20 Hz (Text S1, Video S4) reveals that increased amplitude levels for stations near power lines are highly time dependent. The episodes of increased amplitudes, usually over tens of minutes, are spatially coherent. That is, if nearby power lines induce increased amplitudes on seismometers, they do so along a section that is at least a few kilometers long. The spectrogram (Fig. 5f) shows such an example of increasing amplitudes over minutes, with a few continuous spectral peaks and the onset of an additional spectral peak (all between 10 and 50 Hz). In contrast to windmills, amplitude levels do not appear to coincide with a shift in dominant frequency.

People sometimes report hearing a hissing or cracking sound near power lines, an effect known as corona discharge that can cause audible noise as it ionizes the air around the power line (Loeb, 1965). This effect is certainly relevant at higher, audible frequencies, but may also induce infrasound ($f < 20$ Hz) that could couple seismoacoustically into the ground and seismometers (e.g., Evers *et al.*, 2007; Schneider *et al.*, 2018). Another possible mechanism is mechanical interaction of the transmission towers (spaced at ~300 m in the study area) with the ground and propagation of seismic surface waves from the tower to the seismometers. Transmission towers are certainly vibrating due to interaction with wind. However, any naturally induced mechanism is unlikely to explain continuous spectral lines with constant frequency (Fig. 5f). Indeed, wind speed and precipitation data from a meteorological station in the array reveal that there appears to be no connection between increased seismic amplitudes near power lines at 8–20 Hz and increased wind speed (see Text S1 and supplemental material). Instead, these observations point to seismoacoustic coupling of corona discharge, in which higher electric energy transfer along a section of the power grid could induce more sound and thus increased seismic amplitudes. This is further supported by a section of cross-correlation functions (CCFs) perpendicular to a power line (Fig. S4). The dominant signal that emerges in the CCFs at 10–20 Hz propagates with acoustic velocities.

At 50 Hz, amplitudes decay with $r^{-1.1}$ when considering stations near power lines that are in at least 400 m distance from any other source (Fig. 4). However, when excluding those stations that do not exhibit increased amplitudes near power lines, amplitudes decay with $r^{-2.5}$ (gray line in Fig. 4). This points to spherical propagation, suggesting that seismoacoustic coupling is a likely mechanism. Those stations that do not show increased amplitudes near the power line are located almost exclusively at the southernmost power line in our study area (Fig. 2d), indicating that this power line has potentially been inactive during the deployment.

Gas pipelines

Several gas pipelines cross the study region, transferring gas to and from one of Europe's largest gas hubs—the Baumgarten gas hub (Fig. 2d). Although the gas hub itself is a clear source of seismic energy (Fig. 2b,c), our findings on the gas pipelines themselves are less conclusive. For the stations near the gas hub, only very little data are available (Fig. 1).

We do not find clearly increased amplitudes near gas pipelines (Fig. 2). PSDs that are corrected for cross-contamination (Fig. S2g), however, suggest that we do, in fact, observe slightly increased amplitudes at around 3–11 Hz, compared to no

known nearby sources (Fig. S2h). There is a slight separation of amplitudes that shows roughly two maxima at this frequency range. We find that the stations with higher amplitudes are located toward the west of the study area, near Gänserndorf. In the maps of amplitude levels, we have probably overlooked this effect due to many nearby sources (Fig. 2). This further suggests that the increased amplitude levels between 3 and 11 Hz are indeed not related to the gas pipelines, but to other strong sources more than 400 m away. In fact, we do not find a clear distance dependency at 10 Hz or any other frequency (Fig. 4).

In principle, the flow of gas through pipelines should generate at least some pipe motion. However, friction between the gas and the pipe walls is expected to be very low, for laminar flow. If one could record gas pipeline activity with seismometers, monitoring of pipeline health becomes an attractive prospect. For high resolution, distributed acoustic sensing could be utilized to get low-cost and high-resolution measurements of the pipes' state in real time (Zhan, 2019). At this point, the signal level seems to be quite low though.

Airplanes

The array recorded airplanes traveling to and from the Vienna International Airport, the 14th largest airport in Europe. The airport is located ~25 km to the south-southwest of the center of the study area. Airplanes generate unique high-frequency signals with clear and distinct Doppler effect (Fig. 5i). Meng and Ben-Zion (2018) described the spectral features of air traffic, as recorded on seismograms in great detail, and our measurements have striking resemblance to their observations and modeling of moving airplanes. We do observe a first overtone for all airplanes (e.g., Fig. 5i), a feature that Meng and Ben-Zion (2018) did not observe for all events. Air traffic signals have to couple seismoacoustically into the ground and seismometers; there is no other reasonable mechanism. The fact we record these signals so clearly indicates the potential of this mechanism for seismoacoustic research. The acoustic waves that have been generated primarily have been converted into seismic waves, which we observe. Acoustic–seismic coupling as observed here is currently a topic of research, and these observations can very well help to further understand this phenomenon (e.g., Schneider *et al.*, 2018; Fuchs *et al.*, 2019).

Impact on Green's function retrieval

The aforementioned sources may have significant impact on the retrieval of empirical Green's functions from cross correlations of the ambient seismic field. In particular, windmills act as stationary seismic sources that emit energy continuously, a property they share with ocean-generated noise. Such stationary seismic sources inside of the array likely introduce additional strong arrivals in CCFs, as the assumption of a scattered wavefield or uniform source distribution is clearly violated. Still, these CCFs could be sensitive to the subsurface structure and may certainly be useful for monitoring applications at frequencies above the microseismic frequency band. When aiming at extracting estimated Green's functions from CCFs for imaging purposes, however, these additional arrivals may dominate the signal, and identifying the phase related to direct interstation wave propagation may prove challenging. Roux *et al.* (2016) used double beamforming to filter the extracted wavefield in CCFs to only allow for certain wavenumbers and thus propagation directions. They used this approach to extract surface waves from a body-wave-dominated wavefield. Such an approach should allow to filter out waves propagating from the location of the windmills, at least for some station pairs, potentially enabling subsurface-imaging based on interstation surface-wave velocities even in the presence of strong continuous sources.

Conclusions

We demonstrate that dense seismic arrays allow unique and detailed insight into the spatiotemporal properties of the ambient seismic field at frequencies above the microseisms. Our results complement previous work by other authors on other arrays and some of the sources we observe. We investigate seismic data of an array of 10,532 stations deployed in the eastern Vienna basin for 1 week. Sources of seismic energy that we observe and describe include windmills of different types, a railway track, trains, oil pumpjacks, cars, power lines, and air traffic. All sources exhibit distinctly different spectral and temporal features that allow to describe them and possible to identify them (automatically).

We find that at frequencies most relevant to imaging of shallow subsurface structure with ambient-noise-based surface waves (up to ~10 Hz), windmills, the railway track, and oil pumpjacks emerge as the primary sources of seismic energy in the study area. Windmills, in particular, act as stationary sources that continuously emit strong seismic energy and may introduce unwanted secondary wavefields in ambient noise CCFs. Oil pumpjacks exhibit similar properties, but are less dominant in the seismic records. Because of the high station density, we can fit the amplitude decay with distance at different frequencies and give indications for the propagation regimes of different source-induced wavefields and thus their coupling mechanisms. Windmills, potentially couple by directly shaking the ground at frequencies around 1 Hz, while coupling seismoacoustically at higher frequencies, indicated by spherical amplitude decay. Similarly, power lines also appear to couple seismoacoustically at the power grid frequency and below due to corona discharge.

This study is intended to motivate further studies on this dataset, which may include ambient-noise-based surface-wave tomography, extraction of body waves from the ambient seismic field, and signal detection and identification, as well as seismoacoustics.

Data and Resources

Seismograms used in this study were collected using an array for industrial exploration by OMV E&P GmbH. They can be made available upon request to OMV E&P GmbH. The supplemental material includes animated videos of amplitude levels over time, as well as some observations on nonanthropogenic sources, and the station classification used in this study. Meteorological data from the station Zwerndorf have been provided by Manfred Dorninger. The software used in this study was kindly provided by Beyreuther *et al.* (2010) and Virtanen *et al.* (2020). The colormap used for illustrations in this study was provided by Crameri (2018).

Acknowledgments

The authors thank OMV E&P GmbH for access to the seismic data and the permission to publish these results. Part of this work was performed using funding from the Austrian Science Fund (FWF): Projects 26391 and 30707. The authors thank two anonymous reviewers for their constructive comments that helped improve the article. The authors are grateful to Florian Fuchs, Petr Kolínský, Andrew Delorey, Artemii Novoselov, Manfred Dorninger, and Dimitri Zigone for insightful comments and discussions.

References

Ardhuin, F., E. Stutzmann, M. Schimmel, and A. Mangeney (2011). Ocean wave sources of seismic noise, *J. Geophys. Res.* **116,** C09004, 1–21.

Beyreuther, M., R. Barsch, L. Krischer, T. Megies, Y. Behr, and J. Wassermann (2010). Obspy: A python toolbox for seismology, *Seismol. Res. Lett.* **81,** no. 3, 530.

Brenguier, F., P. Boue, Y. Ben-Zion, F. Vernon, C. W. Johnson, A. Mordret, O. Coutant, P. E. Share, E. Beaucé, D. Hollis, *et al.* (2019). Train traffic as a powerful noise source for monitoring active faults with seismic interferometry, *Geophys. Res. Lett.* **46,** no. 16, 9529–9536.

Brenguier, F., F. Brenguier, R. Courbis, A. Mordret, X. Campman, P. Boue, P. Boué, M. Chmiel, T. Takano, T. Lecocq, *et al.* (2020). Noise-based ballistic wave passive seismic monitoring. Part 1: Body waves, *Geophys. J. Int.* **221,** no. 1, 683–691.

Brenguier, F., M. Campillo, C. Hadziioannou, N. M. Shapiro, R. M. Nadeau, and E. Larose (2008). Postseismic relaxation along the San Andreas fault at Parkfield from continuous seismological observations, *Science* **321,** no. 5895, 1478–1481.

Brenguier, F., M. Campillo, T. Takeda, Y. Aoki, N. M. Shapiro, X. Briand, K. Emoto, and H. Miyake (2014). Mapping pressurized volcanic fluids from induced crustal seismic velocity drops, *Science* **345,** no. 6192, 80–82.

Brix, F., and O. Schultz (1993). *Erdöl und Erdgas in Österreich*, Naturhistorisches Museum Wien and F. Berger, Horn, Wien (in German).

Chamarczuk, M., Y. Nishitsuji, M. Malinowski, and D. Draganov (2019). Unsupervised learning used in automatic detection and classification of ambient-noise recordings from a large-*N* array, *Seismol. Res. Lett.* **91,** no. 1, 370–389.

Crameri, F. (2018). Geodynamic diagnostics, scientific visualisation and StagLab 3.0, *Geosci. Model Dev.* **11,** no. 6, 2541–2562.

de Ridder, S. A. L., and B. L. Biondi (2015). Ambient seismic noise tomography at Ekofisk, *Geophysics* **80,** no. 6, B167–B176.

Dybing, S. N., A. T. Ringler, D. C. Wilson, and R. E. Anthony (2019). Characteristics and spatial variability of wind noise on near-surface broadband seismometers, *Bull. Seismol. Soc. Am.* **109,** no. 3, 1082–1098.

Edwards, W. N. (2015). *Analysis of measured wind turbine seismic noise generated from the Summerside wind farm, Prince Edward Island, Geol. Surv. Canada, Tech. Rept. 7763.*

Evers, L. G., L. Ceranna, H. W. Haak, A. Le Pichon, and R. W. Whitaker (2007). A seismoacoustic analysis of the gas-pipeline explosion near Ghislenghien in Belgium, *Bull. Seismol. Soc. Am.* **97,** no. 2, 417–425.

Fuchs, F., G. Bokelmann, and the AlpArray Working Group (2017). Equidistant spectral lines in train vibrations, *Seismol. Res. Lett.* **89,** no. 1, 56–66.

Fuchs, F., F. M. Schneider, P. Kolínský, S. Serafin, and G. Bokelmann (2019). Rich observations of local and regional infrasound phases made by the AlpArray seismic network after refinery explosion, *Sci. Rep.* **9,** no. 13027, 1009.

Garden, M., and L. Zühlsdorff (2019). Acquisition of a modern seismic survey in the Vienna Basin, *SEG Technical Program*, Expanded Abstracts, Society of Exploration Geophysicists, San Antonio, Texas, September 2019, 253–257.

Gas Connect Austria GmbH (2020). Location of gas pipelines, available at https://www.gasconnect.at/netzinformationen/unser-netz-im-detail/ (last accessed March 2020).

Gortsas, T. V., T. Triantafyllidis, S. Chrisopoulos, and D. Polyzos (2017). Numerical modelling of micro-seismic and infrasound noise radiated by a wind turbine, *Soil Dynam. Earthq. Eng.* **99,** 108–123.

Hasselmann, K. (1963). A statistical analysis of the generation of microseisms, *Rev. Geophys. Space Phys.* **1,** 177–210.

Heténi, G., I. Molinari, J. Clinton, G. Bokelmann, I. Bondár, W. C. Crawford, J.-X. Dessa, C. Doubre, W. Friederich, F. Fuchs, *et al.* (2018). The AlpArray seismic network: A large-scale European experiment to image the alpine Orogen, *Surv. Geophys.* **39,** no. 5, 1–25.

Hu, W., R. J. Barthelmie, F. Letson, and S. C. Pryor (2019). Seismic noise induced by wind turbine operation and wind gusts, *Seismol. Res. Lett.* **91,** no. 1, 427–437.

Inbal, A., T. Cristea Platon, J.-P. Ampuero, G. Hillers, D. Agnew, and S. E. Hough (2018). Sources of long-range anthropogenic noise in southern California and implications for tectonic tremor detection, *Bull. Seismol. Soc. Am.* **108,** no. 6, 3511–3527.

Interessengemeinschaft Windkraft Österreich (2020). A map of windmills, available at https://www.igwindkraft.at/?xmlval_ID_KEY[0]=1055/ (last accessed March 2020).

Johnson, C. W., H. Meng, F. Vernon, and Y. Ben-Zion (2019). Characteristics of ground motion generated by wind interaction with trees, structures, and other surface obstacles, *J. Geophys. Res.***124,** no. 8, 8519–8539.

Juretzek, C., and C. Hadziioannou (2016). Where do ocean microseisms come from? A study of Love-to-Rayleigh wave ratios, *J. Geophys. Res.* **121,** no. 9, 6741–6756.

Juretzek, C., and C. Hadziioannou (2017). Linking source region and ocean wave parameters with the observed primary microseismic noise, *Geophys. J. Int.* **211,** no. 3, 1640–1654.

Karplus, M., and B. Schmandt (2018). Preface to the focus section on geophone array seismology, *Seismol. Res. Lett.* **89,** no. 5, 1597–1600.

Kästle, E. D., A. El-Sharkawy, L. Boschi, T. Meier, C. Rosenberg, N. Bellahsen, L. Cristiano, and C. Weidle (2018). Surface wave tomography of the alps using ambient-noise and earthquake phase velocity measurements, *J. Geophys. Res.* **123,** no. 2, 1770–1792.

Kong, Q., D. T. Trugman, Z. E. Ross, M. J. Bianco, B. J. Meade, and P. Gerstoft (2018). Machine learning in seismology: Turning data into insights, *Seismol. Res. Lett.* **90,** no. 1, 3–14.

Lecocq, T., L. Longuevergne, H. A. Pedersen, F. Brenguier, and K. Stammler (2017). Monitoring ground water storage at mesoscale using seismic noise: 30 years of continuous observation and thermo-elastic and hydrological modeling, *Sci. Rep.* **7,** no. 1, 1–16.

Lin, F. C., M. P. Moschetti, and M. H. Ritzwoller (2008). Surface wave tomography of the western United States from ambient seismic noise: Rayleigh and Love wave phase velocity maps, *Geophys. J. Int.* **173,** no. 1, 281–298.

Loeb, L. B. (1965). *Electrical Coronas, Their Basic Physical Mechanisms*, University of California Press, Berkley, California.

Longuet-Higgings, M. S. (1950). A theory of the origin of microseisms, *Phil. Trans. Roy. Soc. Lond. A* **243,** no. 857, 1–35.

Lu, Y., L. Stehly, A. Paul, and the AlpArray Working Group (2018). High-resolution surface wave tomography of the European crust and uppermost mantle from ambient seismic noise, *Geophys. J. Int.* **214,** no. 2, 1136–1150.

Meng, H., and Y. Ben-Zion (2018). Characteristics of airplanes and helicopters recorded by a dense seismic array near Anza California, *J. Geophys. Res.* **123,** no. 6, 4783–4797.

Mordret, A., R. Courbis, F. Brenguier, M. Chmiel, S. Garambois, S. Mao, P. Boué, X. Campman, T. Lecocq, W. Van der Veen, *et al.* (2020). Noise-based ballistic wave passive seismic monitoring – Part 2: surface waves, *Geophys. J. Int.* **221,** no. 1, 692–705.

Mordret, A., M. Landès, N. M. Shapiro, S. C. Singh, P. Roux, and O. I. Barkved (2013). Near-surface study at the Valhall oil field from ambient noise surface wave tomography, *Geophys. J. Int.* **193,** no. 3, 1627–1643.

Mordret, A., P. Roux, P. Boué, and Y. Ben-Zion (2018). Shallow 3-D structure of the San Jacinto fault zone revealed from ambient noise imaging with a dense seismic array, *Geophys. J. Int.* **216,** no. 2, 1–21.

Nakata, N., J. P. Chang, J. F. Lawrence, and P. Boué (2015). Body wave extraction and tomography at Long Beach, California, with ambient-noise interferometry, *J. Geophys. Res.* **120,** no. 2, 1159–1173.

Nakata, N., L. Gualtieri, and A. Fichtner (Editors) (2019). *Seismic Ambient Noise*, First Ed., Cambridge University Press, Cambridge, United Kingdom.

OpenStreetMap Contributors (2017). Planet dump, available at https://planet.osm.org, https://www.openstreetmap.org (last accessed November 2019).

Ren, Y., B. Grecu, G. Stuart, G. Houseman, E. Hegedüs, and South Carpathian Project Working Group (2013). Crustal structure of the Carpathian–Pannonian region from ambient noise tomography, *Geophys. J. Int.* **195,** no. 2, 1351–1369.

Riahi, N., and P. Gerstoft (2015). The seismic traffic footprint: Tracking trains, aircraft, and cars seismically, *Geophys. Res. Lett.* **42,** no. 8, 2674–2681.

Roux, P. (2009). Passive seismic imaging with directive ambient noise: Application to surface waves and the San Andreas fault in Parkfield, CA, *Geophys. J. Int.* **179,** no. 1, 367–373.

Roux, P., L. Moreau, A. Lecointre, G. Hillers, M. Campillo, Y. Ben-Zion, D. Zigone, and F. Vernon (2016). A methodological approach towards high-resolution surface wave imaging of the San Jacinto Fault Zone using ambient-noise recordings at a spatially dense array, *Geophys. J. Int.* **206,** no. 2, 980–992.

Schippkus, S., D. Zigone, G. Bokelmann, and the AlpArray Working Group (2018). Ambient noise tomography of the wider Vienna basin region, *Geophys. J. Int.* **215,** no. 1, 102–117.

Schneider, F. M., F. Fuchs, P. Kolínský, E. Caffagni, S. Serafin, M. Dorninger, G. Bokelmann, and A. W. Group (2018). Seismo-acoustic signals of the Baumgarten (Austria) gas explosion detected by the AlpArray seismic network, *Earth Planet. Sci. Lett.* **502,** 104–114.

Spica, Z. J., N. Nakata, X. Liu, X. Campman, Z. Tang, and G. C. Beroza (2018). The ambient seismic field at Groningen gas field: An overview from the surface to reservoir depth, *Seismol. Res. Lett.* **89,** no. 4, 1450–1466.

Stammler, K., and L. Ceranna (2016). Influence of wind turbines on seismic records of the Gräfenberg array, *Seismol. Res. Lett.* **87,** no. 5, 1075–1081.

Virtanen, P., R. Gommers, T. E. Oliphant, M. Haberland, T. Reddy, D. Cournapeau, E. Burovski, P. Peterson, W. Weckesser, J. Bright, *et al.* (2020). SciPy 1.0: Fundamental algorithms for scientific computing in Python, *Nat. Methods* **17,** no. 3, 261–272.

Zhan, Z. (2019). Distributed acoustic sensing turns fiber-optic cables into sensitive seismic antennas, *Seismol. Res. Lett.* **91,** no. 1, 1–15.

Manuscript received 28 April 2020
Published online 29 July 2020